Analysis of the Water Adsorption Isotherms in UiO-based Metal-Organic Frameworks

Mason C. Lawrence† and Michael J. Katz*,†

†Department of Chemistry, Memorial University of Newfoundland, St. John's Newfoundland, A1B 3X7

KEYWORDS Metal Organic-Frameworks, Water Adsorption, Gas Adsorption, Pore Size Distribution

ABSTRACT: The present work takes a detailed look at the adsorption of nitrogen gas and water vapour in six related zirconium-based metal-organic frameworks (UiO-66, UiO-66-NH_2, UiO-67, UiO-67-NH_2, UiO-68-Me_4/PCN-57, and UiO-68-NH_2). The work relates the role of defects, linker length, and linker functionality on the gas adsorption properties. The water adsorption isotherms showed no hysteresis consistent with capillary condensation. This suggests a node-based cluster growth mechanism is occurring. Analysis of the water adsorption isotherms illustrated that prior to the water condensation step in the isotherm, each MOF adsorbed roughly 1 water molecule per zirconium centre. As the linker length increases, the MOF becomes more hydrophobic. The amine functionality increases the hydrophilicity, but the effect of the functional group diminishes as the linker length increase. The latter point is illustrated by calculating the apparent contact angle between the pore wall and condensed water. The apparent contact angle increased from 54.0 ° to 83.1 ° from UiO-66 to UiO-68-Me_4/PCN-57 and from 13.0 ° to 71.0 ° from UiO-66-NH_2 to UiO-68-NH_2. From this, the water isotherm was used to construct a pore size distribution consistent with the distribution determined from nitrogen gas adsorption. We further explored the amine-unfunctionlized MOFs for long-term water exposure. Below the water condensation step, the MOFs showed no change in nitrogen gas adsorption capacity/surface area for 100 days.

1 Introduction

Combining metal cations (nodes) with bridging organic ligands (linkers) yields three-dimensional porous materials known as metal-organic frameworks (MOFs). With judicial choice of both node and linker, many different topologies of porous materials can be formed.[1] It is no surprise that the tunability of linkers and nodes has led to MOFs with applications such as gas storage and separations,[2-6] catalysis,[7-10] sensing,[11-12] drug delivery,[13-14] reduction of greenhouse gases,[15] and photo switching materials,[16] to name a few.[11, 17-19]

One area that has received a great deal of interest in recent years is the adsorption and subsequent release/collection of water vapour.[20-25] This has implications in harvesting water from the air in both indoor and outdoor environments. Outdoors, harvesting water from the environment can enable economic growth by providing water for agricultural-related products. Additionally, providing potable water has direct implications on human health. Indoors, maintaining the relative humidity (RH) of a building between 30 – 60% is ideal to reduce mold while maintaining comfort. Heating, ventilation, and air conditioning systems (HVAC) are energy intensive, requiring up to 50% of the industrial and 31% of the residential building energy consumption.[26-27] If a passive system that is capable of maintaining the humidity levels can be found, then HVAC costs could be greatly reduced.

In addition to water harvesting applications, water adsorption in MOFs can be used in heat transformation applications. This relies on the thermodynamics of adsorption/desorption. Heat is required to break adsorbent-adsorbate interactions. If the associated enthalpy can be provided by the temperature associated with a hot room, then the air is cooled by heat transfer to the desorption process. The reverse process can also be performed. Given that the formation of the adsorbent-adsorbate interaction is exothermic, the heat emitted by the adsorption process can be transferred to a cold air stream. Thus, the air is heated by the adsorption process. Given the high density of adsorption sites in a MOF, there is considerable potential for MOFs to be employed in heat transformation processes. [28-30]

In addition to the direct applications of water adsorption, there are several indirect applications associated with water adsorption. For example, water has the potential to act as a competitive inhibitor when other gasses (e.g., CO_2, CH_4)[31] are being adsorbed. This decreases the efficacy of the MOF. Alternatively, water can act as a promotor, assisting in adsorption/desorption processes via hydrogen bonding.[15] It is thus important to understand water adsorption in MOFs.

With regards to water vapour adsorption in MOFs, there are three different water-adsorption mechanisms.[20, 32-33] Capillary condensation, occurs when a monolayer of water is deposited evenly onto the walls of the MOF. Subsequently, water multilayers form before condensation, where the opposite sides of the wall connect, and no further water can be adsorbed. This method is recognized by a water adsorption/desorption isotherm that contains considerable hysteresis in the adsorption vs. desorption step. Around room temperature, capillary condensation occurs in pores that are greater than 2 nm in width.[32] The second mechanism of water adsorption is adsorption and growth of water clusters onto a nucleation site (often, but not necessarily, the node of the MOF). The water clusters grow with increasing water vapour content (partial pressure/relative humidity) until they cannot grow any further. This is often recognized by isotherms that do not have hysteresis in the water vapour adsorption isotherms. The final pathway occurs for very hydrophobic MOFs where a water cluster forms in the pore, without contact with the surface, and grows until the pore is fillled.[34]

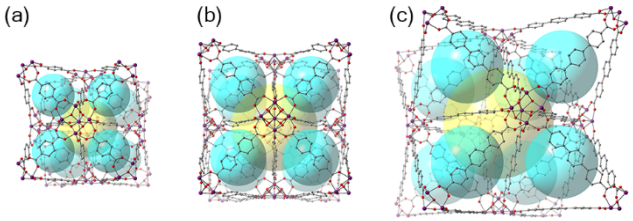

Figure 1: (a) UiO-66 (b) UiO-67 (c) UiO-68. Yellow and blue spheres illustrate the large octahedral pore and smaller tetrahedral pore respectively.

In the present work, we turn our attention to six MOFs that differ in the linker length, linker functionality, and defect density while maintaining the topology of the material. The MOFs investigated herein are the UiO-family (Figure 1) that contain $Zr_6O_4(OH)_4^{12+}$ nodes linked via six, assuming no defects, linear ditopic dicarboxylate-based linkers. These linkers form a large octahedral pore, and a smaller tetrahedral pore. For this work, we selected three unfunctionalized MOFs (UiO-66, UiO-67, and UiO-68-Me_4/PCN-57) and three functionalized MOFs (UiO-66-NH_2, UiO-67-NH_2, and UiO-68-NH_2). The amine-functionalized UiOs were specifically chosen due to the multitude of applications where the amine-functionality enhances the properties of the MOF, or is otherwise utilized to introduce new functional groups into the pore of the MOF.[35-37] By keeping the topology the same, the role of linker length and functionality can lead to a general trend that can be applied to other MOF systems.

2 Experimental

2.1 Synthesis

The linkers for UiO-68-Me_4/PCN-57 (2',3',5',6'-tetramethyl-[1,1':4',1''-terphenyl]-4,4''-dicarboxylic acid; Me_4-H_2TPDC)[38] and UiO-68-NH_2 (2′-amino-1,1′:4,1′′-terphenyl-4,4′′-dicarboxylic acid; NH_2-H_2TPDC)[39] were synthesized via modified literature procedures (see supporting information (SI) for further details).

UiO-66, UiO-66-NH_2, UiO-67, and UiO-67-NH_2, were synthesized according to literature procedures.[40-41] UiO-68-Me_4/PCN-57 and UiO-68-NH_2 was synthesized via a modified literature procedure (see SI for further details).

2.2 Gas Adsorption Studies

Excluding UiO-67-NH_2, prior to gas adsorption measurements, samples were activated on a Micrometrics Smart VacPrep by heating at a rate of 5 K/min to 363 K and holding at this temperature for 30 min under vacuum. Subsequently, the sample was heated to 423 K at 5 K/min and held for 600 min under vacuum. UiO-67-NH_2 was activated by first exchanging the synthesis solvent with ethanol over several days and subsequently activated by supercritical drying using a Tousimis Samdri-PVT-3D supercritical drier. [40, 42-43]

Water isotherms were measured at 295 K on a Micrometrics 3Flex instrument. In order to expose the sample to water vapour, a 3Flex sample holder containing 5 mL of distilled, deionized water was installed on one of the three sample ports and subsequently used as a dosing port. Prior to analysis, the water was subjected to three freeze-pump-thaw cycles to remove any dissolved gases.

3 Results and discussion

The UiO family of MOFs contains an octahedral and a tetrahedral pore in a ratio of 1:2.[44] It has been computationally determined for pristine MOFs containing no defects that the tetrahedral pores increase in width from 3.8 Å to 5.5 Å to 9.7 Å as the linker increases in length from UiO-66 to UiO-67 to UiO-68. Similarly, the larger octahedral pore increases in width from 8.0 Å to 13.1 Å to 17.2 Å.[43] To validate the formation of our MOFs, we measure the powder X-ray diffractograms of the materials (Figure S22-24 in the SI). In all six cases, the observed X-ray diffractograms were consistent with the simulated structures.

3.1 Nitrogen Adsorption Isotherms

To further validate our MOFs, nitrogen gas adsorption isotherms were measured at 77 K and their surface areas and pore size distributions determined (Figure 2, Table 1, Figure S1-S3, and Tables S1-S3 in the SI).

Table 1: MOF characterization data.

	BET Surface Area (m^2/g)		Ligands per formula Unit	Molecular Weight (g/mol)
MOF	Observed	Literature	Observed	$Zr_6O_4(OH)_4L_{6-x}(d^a)_{2x}$
UiO-66	1480	1580[40]	4.8 ± 0.2	1550 ± 30
UiO-66-NH_2	1100	1200[40]	3.8 ± 0.2	1510 ± 40
UiO-67	2500	2500[40]	5.1 ± 0.2	1970 ± 50
UiO-67-NH_2	2000	2080[40]	3.9 ± 0.2	1820 ± 50
UiO-68-Me_4/PCN-57	3475	3300[45]	5.4 ± 0.1	2730 ± 40
UiO-68-NH_2	3350	3750[46]	5.4 ± 0.1	2510 ± 30

As shown in Table 1, the MOFs exhibit nitrogen gas accessible Brunauer–Emmett–Teller (BET) gravimetric surface areas consistent with literature values. As the linker length increases, so does the accessible surface area. The effect of the amine functionality is more difficult to assess. Assuming a MOF with the same number of ligands, the added pendant group provides increased molecular weight, which will lower the gravimetric surface area, and a larger surface for the gas molecules to adsorb onto, which will increase the surface area. These features will have opposing, but not necessarily equal, effects. However, any changes in the number of defects (i.e., missing linkers in UiOs)[47-48] will further impact the surface area; more defects will lower surface area, but the lower molecular weight will make the gravimetric surface area increase. With this in mind, we examined the number of missing linkers by thermogravimetric analysis (TGA).[49] As shown in Table 1, we determined that UiO-66 and UiO-67 contained roughly 1 more linker per formula unit than their amine-functionalized counterparts. With roughly similar molecular weights (1550 g/mol vs 1510 g/mol for UiO-66 and UiO-66-NH_2, respectively) the decrease in surface area is due to a decrease in available surface area for gases to adsorb onto rather than simply a gravimetric change due to a change in molecular weight.[50] This is similarly observed for UiO-67 and UiO-67-NH_2 in which the increased number of defects lowers the observed surface area. This is further confirmed by examining the BET surface area for UiO-68-Me_4/PCN-57 and UiO-68-NH_2 that reflect small changes in accessible surface area caused by the opposing effect of the linker surface area and molecular weight changes.[39, 45]

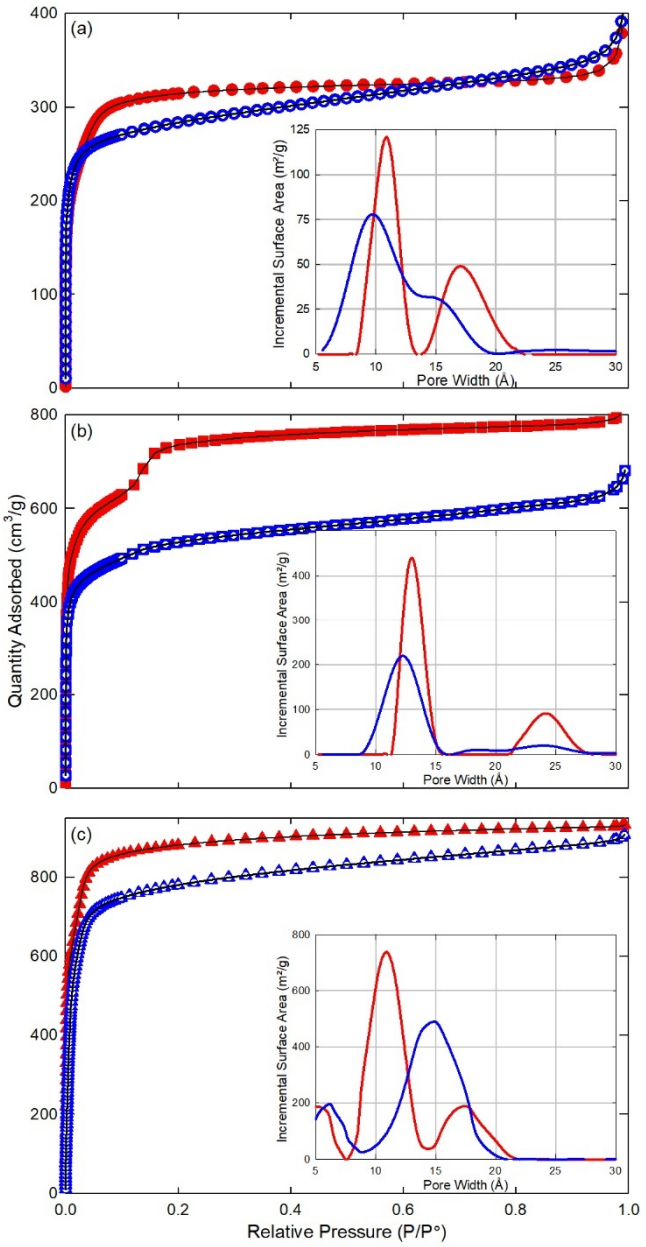

Figure 2: Nitrogen gas adsorption isotherms at 77K of (a) UiO-66 and UiO-66-NH_2 (red and blue trace respectively). (b) UiO-67 and UiO-67-NH_2 (red and blue trace respectively). (c) UiO-68-Me_4/PCN-57 and UiO-68-NH_2 (red and blue trace respectively). The insets show the pore size distribution for the respective MOFs. The pore size distribution for UiO-66, UiO-66-NH_2 and UiO-67-NH_2 were fit to the DFT pillared clay model, while UiO-67, UiO-68-NH_2 and UiO-68-Me_4 were fit to the DFT Tarazona model.[51-52] Figure S1-S3 and Table S1-S3 of the SI illustrate the fits and associated errors.

Returning to the gas-adsorption isotherms, the insets in Figure 2 illustrate the pore size distributions for the six MOFs examined in this work. For UiO-66 and UiO-66-NH_2 (inset Figure 2a; Figure S1, Table S1 in the SI), there appears to be two pores. The observed pore widths of UiO-66 are centered around 11 Å and 17 Å with UiO-66-NH_2 appearing at slightly lower widths and with a broader distribution. The smaller pore observed in the nitrogen gas adsorption isotherm of either MOF is consistent with the experimental and computational octahedral pore width of UiO-66.[40, 43, 53] Given the presence of defects in both MOFs (Table 1), the larger pore is due to pores caused by missing linker defects.[40, 53-55] Although it is not uncommon to observe a pore width consistent with the tetrahedral pore in pristine UiO-66,[53] the presence of defects has been demonstrated to reduce the incremental surface area of the tetrahedral pore while increasing the incremental surface area for defect-based pores. At an HCl concentration of 0.75 M, our data for UiO-66 is consistent with the pore size distribution trend observed by Liang et al. when a concentration of 0.92 M was used.[53] The difference between UiO-66 and UiO-66-NH_2 is likely due to the change in the number of defects leading to a broader distribution (Table 1).[56] As with UiO-66 and UiO-66-NH_2, the pore size distributions for UiO-67 (inset Figure 2b, Figure S2, and Table S2 in the SI) and UiO-67-NH_2 exhibit a similar trend. This is not surprising given the identical synthetic pathway used to make these four MOFs. [40]

The pore size distributions for UiO-68-Me_4/PCN-57 and UiO-68-NH_2 are shown in Figure 2c (Figure S3 and Table S3 in the SI). Unlike the other four MOFs discussed in this work, the errors associated with the pore size distribution fits for the nitrogen gas adsorption isotherms are notably worse for UiO-68-Me_4/PCN-57 and UiO-68-NH_2 (Figures S1, S2, S3, and Tables S1, S2, and S3 in the SI). We are thus hesitant to overly interpret these pore size distributions. The pore size distributions of UiO-68-Me_4/PCN-57 exhibits two pores form the nitrogen gas adsorption isotherms. (11 Å and 17.5 Å in width). The amine-functionalized UiO-68-NH_2 illustrates only one dominant pore centered around 15 Å wide. This pore is consistent with the octahedral pore. [53] Unlike UiO-66 and UiO-67, which have pore widths larger than their amine-functionalized counterparts, UiO-68-Me_4/PCN-57 has an octahedral pore width smaller than UiO-68-NH_2. This is attributed to the larger steric profile of the 4 methyl groups in UiO-68-Me_4/PCN-57. These values are within the range of the previously mentioned computational values.[43]

For all the MOFs, we further probed the argon gas adsorption isotherms, measured at 77K (Figure S25, S26, and S27 in the SI). For UiO-68-Me_4/PCN-57, there is sufficient data to support the presence of the tetrahedral pore at 10 Å). However, for the rest of the MOFs, the pores are either below the limit of the DFT model, or the presence of defects shifts these pore sizes.

3.2 Water Adsorption Isotherms

With the pore characteristics determined, we turned our attention to water adsorption isotherms carried out at 295 K. Figure 2a illustrates the water adsorption isotherms for unfunctionalized MOFs UiO-66, UiO-67, and UiO-68-Me_4/PCN-57, while Figure 3b illustrates the water adsorption isotherms for amine-functionalized MOFs UiO-66-NH_2, UiO-67-NH_2, and UiO-68-NH_2; the data is summarized in Table 2 with the desorption curves available in Figures S4 of the SI. None of the isotherms show a hysteresis loop consistent with capillary condensation.[32] Furthermore, the linkers used are not extremely hydrophobic. Thus, the water adsorption into these MOFs occurs via water cluster formation. Most likely, this cluster growth occurs from the hydrophilic $Zr_6O_4(OH)_4^{12+}$ node. There are three main features associated with these isotherms: the pre pore filling stage, pore filling (condensation), and the post pore-filling adsorption capacity. The results obtained for UiO-66 (Figure 3 red trace) are consistent with previously published results.[47, 53, 57-58] It should be noted that, in this work, UiO-66 shows greater water vapour uptake. This is due to the higher surface area than reported in other works. Previously published UiO-66 water adsorption shows a total uptake of 2.2 mol H_2O/m^2 surface area,[57] normalizing our uptake capacity we obtain 2.1 mol

H_2O/m^2 surface area indicating that our uptakes are in agreement with previously published results.

Table 2: Water Adsorption Data of UiO MOFs

MOF	Adsorption onset (RH)	P_{cond}/P_{sat} (RH)	Adsorption Step Width (RH)
UiO-66	22%	30.95 ± 0.08	18.4± 0.03
UiO-66-NH_2	0%[a]	11.94 ± 0.13	38.3 ± 0.04
UiO-67	47%	52.89 ± 0.08	14.4 ±0.03
UiO-67-NH_2	20%	32.4 ± 0.03 49.9 ± 0.05	24.8 ±0.07 14.0 ± 0.13
UiO-68-Me_4/ PCN-57 [b]	75%	79.00 ±0.03	7.63 ± 0.10
UiO-68-NH_2[b]	36%	32.4 ± 0.03 49.9 ± 0.05	16.8 ± 0.07 23.1 ± 1.4

[a] No water cluster formation region is observed.
[b] See supporting information (Section 2.6) for supplemental discussions.

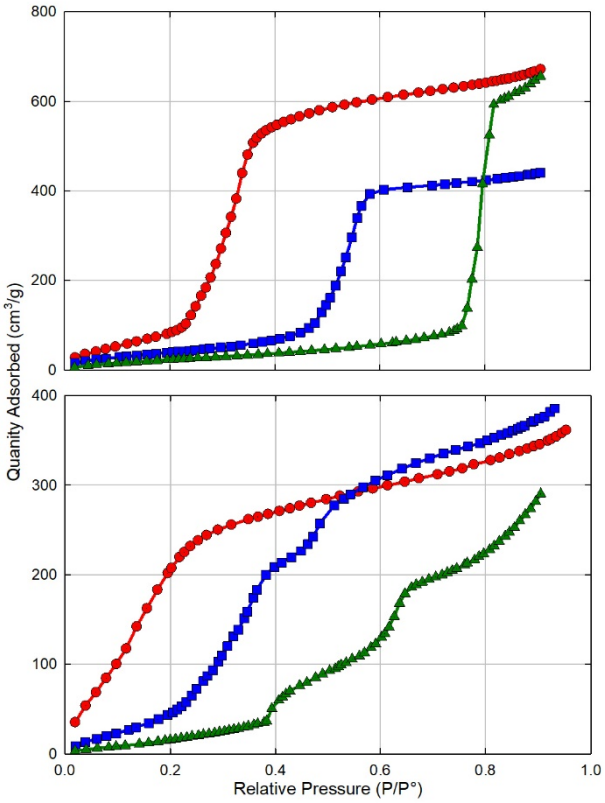

Figure 3: (a) Water isotherms of UiO-66 (circles: red trace), UiO-67 (squares: blue trace), UiO-68-Me_4/PCN-57 (triangles: green trace). (b) Water isotherm of UiO-66-NH_2 (circles: red trace), UiO-67-NH_2 (squares: blue trace) and UiO-68-NH_2 (triangles: green trace)

3.2.1 Pre Pore-Filling

It has been suggested that the pre pore-filling in MOFs is due to node-centered water cluster growth.[58] As illustrated in Figure 3, the pre pore filling stage seems to stop at roughly the same uptake for all six MOFs. Normalizing the water adsorption isotherms for the water:zirconium ratio (Figure S6), we notice that all the MOFs adsorb approximately 1 water molecule per zirconium centre just as condensation starts. Where the MOFs defer is at the relative humidity that this ratio occurs at. This suggests that the water cluster formation stage is dependent on the pore sizes and pore functionality of the MOFs. From an application point of view, these results indicate that as long as the relative humidity remains below the condensation step (pore filling), water can safely co-exist within the MOF and with other analytes in the pore. Extrapolating to larger MOFs, the relative humidity under which advantageous cooperative behaviour/adsorption can occur is expected to increase without risk.

3.2.2 Condensation

With the pre pore-filling adsorption examined, we turned our attention to condensation of water in the pores. For the three unfunctionalized MOFs (UiO-66, UiO-67, and UiO-68-Me_4/PCN-57) and UiO-66-NH_2, the condensation stage occurs in one step. For UiO-67-NH_2, and UiO-68-NH_2, the condensation occurs in two steps. For UiO-67, the second step is due to a small impurity of biphenyldicarboxylate (BPDC) in the 2-aminobiphenyl-4,4'-dicarboxylate (NH_2-BPDC) linker. For UiO-68-NH_2 the relative contribution of the first step depends on the synthetic procedure (see section 2.6 in the SI for further discussion).

$$\ln\left(\frac{P_{cond}}{P_{sat}}\right) = \frac{2V_m\gamma\cos\theta}{r_k RT} \qquad (1)$$

To further ascertain how the pores are changing, we calculated the apparent contact angle of the water inside the pore via the Kelvin equation (Equation 1). The Kelvin equation relates the partial pressure (P_{cond}/P_{sat}) at which the centre of the adsorption step occurs (Table 2 column 3) to the adsorbate properties (the molar volume of liquid water, V_m, and the liquid/vapour surface tension, γ), the adsorbent properties (pore width, r_k), and the interactions between the adsorbent and the adsorbate (the apparent contact angle, θ). While the Kelvin equation is likely an oversimplification of the physical properties inside the MOF, the apparent contact angle facilitates a comparison between different MOFs.

Qualitatively, as the pore size of the MOF increases, the relative pressure associated with pore filling shifts to higher relative humidity. This is consistent with the Kelvin equation, which illustrates that the position of the condensation step (P_{cond}/P_{sat}) shifts to higher relative pressure as the pore width (r_k) increases. Comparing the amine-unfunctionalized MOFs with those of their respective amine-functionalized counterparts, a shift in P_{cond}/P_{sat} to lower relative humidity is observed. Given that the pairs of MOFs (e.g., UiO-66 vs. UiO-66-NH_2) have similar pore size distributions (r_k), the stark difference in water adsorption must be due to a change in the adsorbent adsorbate properties within the pore (θ); unsurprisingly, the amine-functionalized MOFs appear more hydrophilic (smaller apparent contact angle, θ) than their unfunctionalized counter MOFs.

Table 3: Calculated Apparent Contact Angle and Pore Width of UiO MOFs

MOF	Apparent Contact Angle (θ)	Cylindrical Pore Width ($2*r_k$) (Å)
UiO-66	54.0	10.8
UiO-66-NH_2	13.0	9.89
UiO-67	66.5	13.5
UiO-67-NH_2	49.5	12.4
UiO-68-Me_4/PCN-57	83.1	10.8
UiO-68-NH_2	71.0	14.7

Using the pore size distributions from nitrogen gas adsorption isotherms as a measure for the pore width in the Kelvin

Equation (Equation 1, $2*r_k$), and P_{cond}/P_{sat} from the water adsorption isotherms, a quantitative measure of the apparent contact angle (θ) can be calculated (Table 3). Assuming the surface of the framework was perfectly wettable (θ = 0 °), the pore width for UiO-66 would be 18.4 Å. This is considerably larger than the expected pore width from the nitrogen gas adsorption isotherm. This implies that the surface of UiO-66, and the larger MOFs, is not perfectly wettable. Adjusting the apparent contact angle (θ) until the calculated pore width ($2*r_k$ in Equation 1) matches the observed pore size distribution (Figure 2), the apparent contact angle for UiO-66 is estimated to be 54.0 °. The more hydrophilic UiO-66-NH_2 has an apparent contact angle that is 41 ° lower (13.0 °). As the linker length increases, so does the apparent contact angle (Table 3). However, the effect of the amine substituent on the apparent contact angle decreases considerably with increasing pore width (17 ° decrease for UiO-67-NH_2 and a 12.1 ° decrease for UiO-68-NH_2). This suggests a cooperative effect when the amine substituents are in proximity of the node.

The apparent contact angle calculated for these MOFs are consistent with hydrophilic materials. With the exception of UiO-66-NH_2, which borders on a perfectly wettable (θ = 0 ° would yield a dominant pore with of 10.1 Å), the remaining MOFs have apparent contact angles comparable to common organic polymers (e.g., poly(vinyl acetate) = 80 °, polymethyl methacrylate = 68 °, polycarbonate = 88 °).[59-61]

Given the relationship between pore aperture/functionality and the water adsorption isotherms, it is reasonable to conclude that the condensation step should mirror the pore size distribution. Indeed, the breadth of the peak distribution determined from both nitrogen gas and water vapour adsorption are similar (Figure S5 in the SI).

To further look at the adsorption process, we extrapolated the isosteric enthalpies of adsorption for UiO-66 using variable temperature water vapour adsorption. As shown in Figure S7, for water adsorption leading up to $1H_2O$:Zr, the enthalpies are quite high owing to the formation of the first node-OH_2 interaction. Subsequently, the enthalpies reflect the enthalpy of vaporization for water (44 KJ/mol). This is consistent with the data demonstrated above.

3.2.3 Water Adsorption Capacity

In comparison to the nitrogen gas adsorption isotherms, the water adsorption capacity for all the MOFs appears more similar than different. Normalizing the water adsorption isotherms to water per zirconium (Figure S6 in the SI), an interesting observation emerges. The water adsorption isotherms seem to only adsorb 5 (UiO-66-NH_2 and UiO-67, UiO-68-NH_2), 8 (UiO-66, UiO-67-NH_2), or 10 (UiO-68-Me_4/PCN-57) water molecules per zirconium. For UiO-66 and UiO-66-NH_2, the adsorption capacity is consistent with the expected pore volume (10 and 5 water molecules per zirconium). However, for the larger MOFs, the adsorption capacity does not increase to the predicted capacity of >15 water molecules per zirconium (UiO-67-NH_2). This indicates that at linker lengths greater than one phenylene group (UiO-66/UiO-66-NH_2), the water molecules cluster around the node with neighboring clusters not able to connect with each other (Figure 4). It is unclear from this work if water clusters around each node, like a shell, or around each zirconium (Figure 4). We hypothesize that this is around each zirconium rather than each node, but computational work is necessary to tease this out. Of particular note is that there is considerable space remaining in the larger MOFs for other gases to fill the unused volume and interact with the node/water cluster.

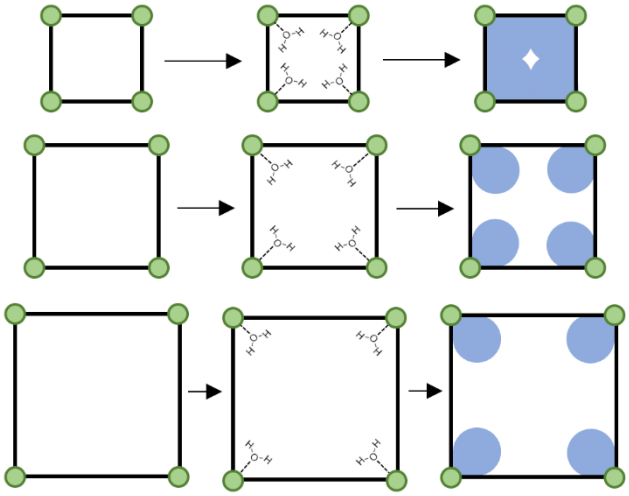

Figure 4: Water adsorption process. Initially empty (left), water molecule is strongly adsorbed onto the node ($1H_2O$/Zr) (middle). Subsequently, a water cluster (5-10 molecules/Zr) grows (right). Green circles represent the $Zr_6O_4(OH)_4$ cluster, black rectangles represent the different length of linker in UiO-66 (top), UiO-67 (middle), UiO-68-Me_4/PCN-57 (bottom).

3.3 Long Term Water Vapour Studies

The obtained data illustrates that water vapour clusters around the node. To ascertain how this affects the MOF, we examined the nitrogen-accessible BET surface area of the amine-unfunctionalized MOFs after expose to water vapour at relative pressures below the pore filling step. Humidity chambers of 25%, 54%, and 75% were made using potassium acetate, magnesium nitrate, and sodium chloride saturated solutions in water. As has been previously demonstrated, and verified herein, when UiO-66 is exposed to 75% humidity for 100 days, the nitrogen-accessible BET surface area remained unchanged.[62] When UiO-67 is exposed to 25% RH for 100 days, the BET accessible surface area is also unchanged. Above the relative pressure associated with pore-filling, where it is well established that UiO-67 cannot be activated from water,[63-66] the expected BET surface area could not be achieved upon thermal activation. We hypothesize that solvent exchange may be used to regenerate the full surface area of the material.[65] With regards to UiO-68-Me_4/PCN-57, at over 100 days at 54% RH there was no significant loss in the surface area (Figure S28). As such, no adverse effects were observed to these MOFs, below the adsorption step.

To further probe this, powder X-ray diffractograms were measured for the six MOFs after water vapour exposure below the step in the isotherm. The data (Figure S22-S24) shows no significant changes for the MOFs explored here. Thus, with larger Zr-based MOFs, which will have adsorption steps at even higher relative humidity, concerns of water vapour are negligible.

To explore the adsorption process further, we also explored the water adsorption isotherm in ever-increasing final relative humidity cycles (Figure S9-S11). For UiO-66, the adsorption/desorption trace does not change as a function of the final relative humidity of each cycle (Figure S19). For UiO-67, below 50% RH, the adsorption/desorption cycles were identical (Figure S10). Adsorption up to 50% RH followed by desorption resulted in a desorption profile that was not reversible. This suggests that heat, solvent exchange, or lower pressures are necessary to remove all the water molecules. However, what is of key importance is that further adsorption from this point leads to adsorption that is consistent with UiO-67. This indicates that

the water molecules that could not desorb did not adversely affect the material over the course of this experiment. For UiO-68-Me_4/PCN-57 (Figure S11), we observed a similar trend as with UiO-67. Interestingly however, the condensation step seems to shift to higher RH as a function of cycles. This is consistent with our exploration of different UiO-68-Me_4/PCN-57 synthetic procedures (See section 2.6 of the SI for further details).

4 Conclusions

Water adsorption onto porous materials shows great promise for removal of water vapour from the air. Simultaneously, for other applications, water vapour adsorption may inhibit or enhance chemistry inside a porous material. The work presented herein presents an in-depth look at zirconium-based MOFs by analyzing the water adsorption isotherms using nitrogen adsorption isotherms as a point of comparison.

Extending our results toward the applications of zirconium-based MOFs, there are three conclusions that can be drawn from our work. Firstly, at relative pressures below the occurrence of condensation, water reversibly adsorbs approximately one water molecule per zirconium centre. This indicates that the porous structure is still capable of adsorbing other gases and may even offer advantageous hydrogen bonding to assist in adsorption, catalysis, and/or chemical reactivity. Furthermore, at these partial pressures, we observed no detrimental effect on these MOFs. Secondly, the hydrophobicity of the pore increases as the pore width increases. These results indicate that zirconium-based MOFs as large or larger than UiO-68 are safe from interference or structural changes at most humidity levels. This is ideal for MOF applications in high humidity environments where we expect water to safely co-exist with the MOF. Lastly, with consideration to HVAC systems, UiO-66 is an ideal candidate for passive HVAC systems. The onset of water adsorption is centered around the ideal indoor air conditions.

ASSOCIATED CONTENT

Supporting information for the synthesis of linkers, synthesis of UiO-68-Me_4/PCN-57, nitrogen gas and argon gas adsorption isotherms with pore size distribution fits, water adsorption and desorption isotherms, comparison of pore size distributions from water and nitrogen gas adsorption isotherms, isosteric enthalpies of adsorption, TGA data and analysis, powder X-ray diffraction, and equations used for water fits can be found free of charge via the Internet at http://pubs.acs.org.

Corresponding Author

Michael J. Katz
Email: mkatz@mun.ca
Department of Chemistry, Memorial University of Newfoundland, St. John's Newfoundland, A1B 3X7

Acknowledgment

The authors would like to acknowledge the Natural Sciences and Engineering Research Council of Canada (NSERC) for funding via the Discovery Grant and Research Tools and Instruments Grant. The Research and Development Corporation of Newfoundland (RDC; now TCII) is gratefully acknowledged for a Leverage Grant. We thank the Core Research Equipment & Instrument Training Network (CREAIT) at Memorial University for the use of their NMR facilities within the Centre for Chemical Analysis, Research and Training (C-CART). MCL would like to acknowledge Qalipu First Nations Post-Secondary Support Program.

REFERENCES

1. Li, M.; Li, D.; O'Keeffe, M.; Yaghi, O. M. Topological Analysis of Metal–Organic Frameworks with Polytopic Linkers and/or Multiple Building Units and the Minimal Transitivity Principle. *Chem. Rev.* **2014,** *114* (2), 1343-1370. DOI: 10.1021/cr400392k
2. Rodenas, T.; Luz, I.; Prieto, G.; Seoane, B.; Miro, H.; Corma, A.; Kapteijn, F.; Llabrés I Xamena, F. X.; Gascon, J. Metal–Organic Framework Nanosheets in Polymer Composite Materials for Gas Separation. *Nat. Mater.* **2014,** *14*, 48. DOI: 10.1038/nmat4113
3. Kong, C.; Du, H.; Chen, L.; Chen, B. Nanoscale MOF/Organosilica Membranes on Tubular Ceramic Substrates for Highly Selective Gas Separation. *Energy Environ. Sci.* **2017,** *10* (8), 1812-1819. DOI: 10.1039/C7EE00830A
4. Nabais, A. R.; Ribeiro, R. P. P. L.; Mota, J. P. B.; Alves, V. D.; Esteves, I. A. A. C.; Neves, L. A. CO_2/N_2 Gas Separation Using Fe(BTC)-Based Mixed Matrix Membranes: A View on the Adsorptive and Filler Properties of Metal-Organic Frameworks. *Sep. Purif. Technol.* **2018,** *202*, 174-184. DOI: 10.1016/j.seppur.2018.03.028
5. Alezi, D.; Belmabkhout, Y.; Suyetin, M.; Bhatt, P. M.; Weseliński, Ł. J.; Solovyeva, V.; Adil, K.; Spanopoulos, I.; Trikalitis, P. N.; Emwas, A.-H.; Eddaoudi, M. MOF Crystal Chemistry Paving the Way to Gas Storage Needs: Aluminum-Based soc-MOF for CH_4, O_2, and CO_2 Storage. *J. Am. Chem. Soc.* **2015,** *137* (41), 13308-13318. DOI: 10.1021/jacs.5b07053
6. Li, L.; Tang, S.; Wang, C.; Lv, X.; Jiang, M.; Wu, H.; Zhao, X. High Gas Storage Capacities and Stepwise Adsorption in a UiO Type Metal–Organic Framework Incorporating Lewis Basic Bipyridyl Sites. *Chem. Commun.* **2014,** *50* (18), 2304-2307. DOI: 10.1039/C3CC48275H
7. Rogge, S. M. J.; Bavykina, A.; Hajek, J.; Garcia, H.; Olivos-Suarez, A. I.; Sepúlveda-Escribano, A.; Vimont, A.; Clet, G.; Bazin, P.; Kapteijn, F.; Daturi, M.; Ramos-Fernandez, E. V.; Llabrés I Xamena, F. X.; Van Speybroeck, V.; Gascon, J. Metal–Organic and Covalent Organic Frameworks as Single-Site Catalysts. *Chem. Soc. Rev.* **2017,** *46* (11), 3134-3184. DOI: 10.1039/C7CS00033B
8. Huang, Y.-B.; Liang, J.; Wang, X.-S.; Cao, R. Multifunctional Metal–Organic Framework Catalysts: Synergistic Catalysis and Tandem Reactions. *Chem. Soc. Rev.* **2017,** *46* (1), 126-157. DOI: 10.1039/C6CS00250A
9. Cardenas-Morcoso, D.; Ifraemov, R.; García-Tecedor, M.; Liberman, I.; Gimenez, S.; Hod, I. A Metal–Organic Framework Converted Catalyst that Boosts Photo-Electrochemical Water Splitting. *J. Mater. Chem. A* **2019,** *7* (18), 11143-11149. DOI: 10.1039/C9TA01559K
10. He, W.; Gao, H.-M.; Shimoni, R.; Lu, Z.-Y.; Hod, I. Synergistic Coupling of Anionic Ligands To Optimize the Electronic and Catalytic Properties of Metal–Organic Framework-Converted Oxygen-Evolving Catalysts. *ACS Appl. Energy Mater.* **2019,** *2* (3), 2138-2148. DOI: 10.1021/acsaem.8b02160
11. Stassen, I.; Burtch, N.; Talin, A.; Falcaro, P.; Allendorf, M.; Ameloot, R. An Updated Roadmap for the Integration of Metal–Organic Frameworks with Electronic Devices and Chemical Sensors. *Chem. Soc. Rev.* **2017,** *46* (11), 3185-3241. DOI: 10.1039/C7CS00122C
12. Lustig, W. P.; Mukherjee, S.; Rudd, N. D.; Desai, A. V.; Li, J.; Ghosh, S. K. Metal–Organic Frameworks: Functional Luminescent and Photonic Materials for Sensing Applications. *Chem. Soc. Rev.* **2017,** *46* (11), 3242-3285. DOI: 10.1039/C6CS00930A
13. Cai, W.; Wang, J.; Chu, C.; Chen, W.; Wu, C.; Liu, G. Metal–Organic Framework-Based Stimuli-Responsive Systems for

Drug Delivery. *Adv. Sci* **2019,** *6* (1), 1801526. DOI: 10.1002/advs.201801526
14. Wu, M.-X.; Yang, Y.-W. Metal–Organic Framework (MOF)-Based Drug/Cargo Delivery and Cancer Therapy. *Adv. Mater.* **2017,** *29* (23), 1606134. DOI: 10.1002/adma.201606134
15. McGrath, D. T.; Ryan, M. D.; MacInnis, J. J.; VandenBoer, T. C.; Young, C. J.; Katz, M. J. Selective decontamination of the reactive air pollutant nitrous acid via node-linker cooperativity in a metal–organic framework. *Chem. Sci.* **2019,** *10* (21), 5576-5581. DOI: 10.1039/C9SC01357A
16. Furlong, B. J.; Katz, M. J. Bistable Dithienylethene-Based Metal–Organic Framework Illustrating Optically Induced Changes in Chemical Separations. *J. Am. Chem. Soc.* **2017,** *139* (38), 13280-13283. DOI: 10.1021/jacs.7b07856
17. Wang, H.; Lustig, W. P.; Li, J. Sensing and Capture of Toxic and Hazardous Gases and Vapors by Metal–Organic Frameworks. *Chem. Soc. Rev.* **2018,** *47* (13), 4729-4756. DOI: 10.1039/C7CS00885F
18. Wang, P.-L.; Xie, L.-H.; Joseph, E. A.; Li, J.-R.; Su, X.-O.; Zhou, H.-C. Metal–Organic Frameworks for Food Safety. *Chem. Rev.* **2019,** *119* (18), 10638-10690. DOI: 10.1021/acs.chemrev.9b00257
19. Dhakshinamoorthy, A.; Li, Z.; Garcia, H. Catalysis and Photocatalysis by Metal Organic Frameworks. *Chem. Soc. Rev.* **2018,** *47* (22), 8134-8172. DOI: 10.1039/C8CS00256H
20. Kalmutzki, M. J.; Diercks, C. S.; Yaghi, O. M. Metal–Organic Frameworks for Water Harvesting from Air. *Adv. Mater.* **2018,** *30* (37), 1704304. DOI: 10.1002/adma.201704304
21. Kim, H.; Yang, S.; Rao, S. R.; Narayanan, S.; Kapustin, E. A.; Furukawa, H.; Umans, A. S.; Yaghi, O. M.; Wang, E. N. Water Harvesting from Air With Metal-Organic Frameworks Powered by Natural Sunlight. *Science* **2017,** *356* (6336), 430-434. DOI: 10.1126/science.aam8743
22. Rieth, A. J.; Yang, S.; Wang, E. N.; Dincă, M. Record Atmospheric Fresh Water Capture and Heat Transfer with a Material Operating at the Water Uptake Reversibility Limit. *ACS Central Science* **2017,** *3* (6), 668-672. DOI: 10.1021/acscentsci.7b00186
23. Rieth, A. J.; Wright, A. M.; Skorupskii, G.; Mancuso, J. L.; Hendon, C. H.; Dincă, M. Record-Setting Sorbents for Reversible Water Uptake by Systematic Anion Exchanges in Metal–Organic Frameworks. *J. Am. Chem. Soc.* **2019,** *141* (35), 13858-13866. DOI: 10.1021/jacs.9b06246
24. Kim, S.-I.; Yoon, T.-U.; Kim, M.-B.; Lee, S.-J.; Hwang, Y. K.; Chang, J.-S.; Kim, H.-J.; Lee, H.-N.; Lee, U. H.; Bae, Y.-S. Metal–Organic Frameworks With High Working Capacities and Cyclic Hydrothermal Stabilities for Fresh Water Production. *Chem. Eng. J.* **2016,** *286*, 467-475. DOI: 10.1016/j.cej.2015.10.098
25. Trapani, F.; Polyzoidis, A.; Loebbecke, S.; Piscopo, C. G. On the General Water Harvesting Capability of Metal-Organic Frameworks Under Well-Defined Climatic Conditions. *Microporous Mesoporous Mater.* **2016,** *230*, 20-24. DOI: 10.1016/j.micromeso.2016.04.040
26. Huang, W. Z.; Zaheeruddin, M.; Cho, S. H. Dynamic Simulation of Energy Management Control Functions for HVAC Systems in Buildings. *Energy Convers. Manage.* **2006,** *47* (7), 926-943. DOI: 10.1016/j.enconman.2005.06.011
27. Wei, X.; Kusiak, A.; Li, M.; Tang, F.; Zeng, Y. Multi-Objective Optimization of the HVAC (Heating, Ventilation, and Air Conditioning) System Performance. *J. Energy* **2015,** *83*, 294-306. DOI: 10.1016/j.energy.2015.02.024
28. Jeremias, F.; Fröhlich, D.; Janiak, C.; Henninger, S. K. Water and methanol adsorption on MOFs for cycling heat transformation processes. *New J. Chem.* **2014,** *38* (5), 1846-1852. DOI: 10.1039/C3NJ01556D
29. Henninger, S. K.; Jeremias, F.; Kummer, H.; Janiak, C. MOFs for Use in Adsorption Heat Pump Processes. *Eur. J. Inorg. Chem.* **2012,** *2012* (16), 2625-2634. DOI: 10.1002/ejic.201101056
30. Henninger, S. K.; Habib, H. A.; Janiak, C. MOFs as Adsorbents for Low Temperature Heating and Cooling Applications. *J. Am. Chem. Soc.* **2009,** *131* (8), 2776-2777. DOI: 10.1021/ja808444z
31. Jasuja, H.; Walton, K. S. Experimental Study of CO_2, CH_4, and Water Vapor Adsorption on a Dimethyl-Functionalized UiO-66 Framework. *J. Phys. Chem. C* **2013,** *117* (14), 7062-7068. DOI: 10.1021/jp311857e
32. Canivet, J.; Fateeva, A.; Guo, Y.; Coasne, B.; Farrusseng, D. Water Adsorption in MOFs: Fundamentals and Applications *Chem. Soc. Rev.* **2014,** *43* (16), 5594-5617. DOI: 10.1039/C4CS00078A
33. Burtch, N. C.; Jasuja, H.; Walton, K. S. Water Stability and Adsorption in Metal–Organic Frameworks. *Chem. Rev.* **2014,** *114* (20), 10575-10612. DOI: 10.1021/cr5002589
34. Nijem, N.; Canepa, P.; Kaipa, U.; Tan, K.; Roodenko, K.; Tekarli, S.; Halbert, J.; Oswald, I. W. H.; Arvapally, R. K.; Yang, C.; Thonhauser, T.; Omary, M. A.; Chabal, Y. J. Water Cluster Confinement and Methane Adsorption in the Hydrophobic Cavities of a Fluorinated Metal–Organic Framework. *J. Am. Chem. Soc.* **2013,** *135* (34), 12615-12626. DOI: 10.1021/ja400754p
35. Peterson, G. W.; Mahle, J. J.; DeCoste, J. B.; Gordon, W. O.; Rossin, J. A. Extraordinary NO_2 Removal by the Metal–Organic Framework UiO-66-NH_2. *Angew. Chem. Int. Ed.* **2016,** *55* (21), 6235-6238. DOI: 10.1002/anie.201601782
36. Bunge, M. A.; Davis, A. B.; West, K. N.; West, C. W.; Glover, T. G. Synthesis and Characterization of UiO-66-NH_2 Metal–Organic Framework Cotton Composite Textiles. *Ind. Eng. Chem. Res.* **2018,** *57* (28), 9151-9161. DOI: 10.1021/acs.iecr.8b01010
37. Ko, N.; Hong, J.; Sung, S.; Cordova, K. E.; Park, H. J.; Yang, J. K.; Kim, J. A Significant Enhancement of Water Vapour Uptake at Low Pressure by Amine-Functionalization of UiO-67. *Dalton Trans.* **2015,** *44* (5), 2047-2051. DOI: 10.1039/C4DT02582B
38. Liu, Y.; Chen, Y.-P.; Liu, T.-F.; Yakovenko, A. A.; Raiff, A. M.; Zhou, H.-C. Selective Gas Adsorption and Unique Phase Transition Properties in a Stable Magnesium Metal-Organic Framework Constructed from Infinite Metal Chains. *CrystEngComm* **2013,** *15* (45), 9688-9693. DOI: 10.1039/C3CE41106K
39. Schaate, A.; Roy, P.; Godt, A.; Lippke, J.; Waltz, F.; Wiebcke, M.; Behrens, P. Modulated Synthesis of Zr-Based Metal–Organic Frameworks: From Nano to Single Crystals. *Chem. Eur. J.* **2011,** *17* (24), 6643-6651. DOI: 10.1002/chem.201003211
40. Katz, M. J.; Brown, Z. J.; Colón, Y. J.; Siu, P. W.; Scheidt, K. A.; Snurr, R. Q.; Hupp, J. T.; Farha, O. K. A Facile Synthesis of UiO-66, UiO-67 and Their Derivatives. *Chem. Commun.* **2013,** *49* (82), 9449-9451. DOI: 10.1039/C3CC46105J
41. Marshall, R. J.; Kalinovskyy, Y.; Griffin, S. L.; Wilson, C.; Blight, B. A.; Forgan, R. S. Functional Versatility of a Series of Zr Metal–Organic Frameworks Probed by Solid-State Photoluminescence Spectroscopy. *J. Am. Chem. Soc.* **2017,** *139* (17), 6253-6260. DOI: 10.1021/jacs.7b02184
42. Howarth, A. J.; Peters, A. W.; Vermeulen, N. A.; Wang, T. C.; Hupp, J. T.; Farha, O. K. Best Practices for the Synthesis, Activation, and Characterization of Metal–Organic Frameworks. *Chem. Mater.* **2017,** *29* (1), 26-39. DOI: 10.1021/acs.chemmater.6b02626
43. Al-Jadir, T. M.; Siperstein, F. R. The Influence of the Pore Size in Metal–Organic Frameworks in Adsorption and Separation of Hydrogen Sulphide: A Molecular Simulation

Study. *Microporous Mesoporous Mater.* **2018,** *271*, 160-168. DOI: 10.1016/j.micromeso.2018.06.002
44. Trotta, F.; Mele, A., *Nanosponges: Synthesis and Applications*. John Wiley & Sons: 2019; p 350.
45. Goswami, S.; Miller, C. E.; Logsdon, J. L.; Buru, C. T.; Wu, Y.-L.; Bowman, D. N.; Islamoglu, T.; Asiri, A. M.; Cramer, C. J.; Wasielewski, M. R.; Hupp, J. T.; Farha, O. K. Atomistic Approach toward Selective Photocatalytic Oxidation of a Mustard-Gas Simulant: A Case Study with Heavy-Chalcogen-Containing PCN-57 Analogues. *ACS Appl. Mater. Interfaces* **2017,** *9* (23), 19535-19540. DOI: 10.1021/acsami.7b07055
46. Carboni, M.; Lin, Z.; Abney, C. W.; Zhang, T.; Lin, W. A Metal–Organic Framework Containing Unusual Eight-Connected Zr–Oxo Secondary Building Units and Orthogonal Carboxylic Acids for Ultra-sensitive Metal Detection. *Chem. Eur. J.* **2014,** *20* (46), 14965-14970. DOI: 10.1002/chem.201405194
47. Ghosh, P.; Colón, Y. J.; Snurr, R. Q. Water Adsorption in UiO-66: The Importance of Defects. *Chem. Commun.* **2014,** *50* (77), 11329-11331. DOI: 10.1039/C4CC04945D
48. Wu, H.; Chua, Y. S.; Krungleviciute, V.; Tyagi, M.; Chen, P.; Yildirim, T.; Zhou, W. Unusual and Highly Tunable Missing-Linker Defects in Zirconium Metal–Organic Framework UiO-66 and Their Important Effects on Gas Adsorption. *J. Am. Chem. Soc.* **2013,** *135* (28), 10525-10532. DOI: 10.1021/ja404514r
49. Shearer, G. C.; Chavan, S.; Bordiga, S.; Svelle, S.; Olsbye, U.; Lillerud, K. P. Defect Engineering: Tuning the Porosity and Composition of the Metal–Organic Framework UiO-66 via Modulated Synthesis. *Chem. Mater.* **2016,** *28* (11), 3749-3761. DOI: 10.1021/acs.chemmater.6b00602
50. Sarkisov, L.; Harrison, A. Computational Structure Characterisation Tools in Application to Ordered and Disordered Porous Materials. *Mol Simul.* **2011,** *37* (15), 1248-1257. DOI: 10.1080/08927022.2011.592832
51. Evans, R.; Marconi, U. M. B.; Tarazona, P. Capillary Condensation and Adsorption in Cylindrical and Slit-Like Pores. *J. Chem. Soc., Faraday Trans. 2* **1986,** *82* (10), 1763-1787. DOI: 10.1039/F29868201763
52. Olivier, J. P.; Occelli, M. L. Surface Area and Microporosity of a Pillared Interlayered Clay (PILC) from a Hybrid Density Functional Theory (DFT) Method. *J. Phys. Chem. B* **2001,** *105* (3), 623-629. DOI: 10.1021/jp001822l
53. Liang, W.; Coghlan, C. J.; Ragon, F.; Rubio-Martinez, M.; D'Alessandro, D. M.; Babarao, R. Defect Engineering of UiO-66 for CO_2 and H_2O Uptake – a Combined Experimental and Simulation Study. *Dalton Trans.* **2016,** *45* (11), 4496-4500. DOI: 10.1039/C6DT00189K
54. Cliffe, M. J.; Wan, W.; Zou, X.; Chater, P. A.; Kleppe, A. K.; Tucker, M. G.; Wilhelm, H.; Funnell, N. P.; Coudert, F.-X.; Goodwin, A. L. Correlated Defect Nanoregions in a Metal–Organic Framework. *Nat. Commun.* **2014,** *5*, 4176. DOI: 10.1038/ncomms5176
55. Shan, B.; McIntyre, S. M.; Armstrong, M. R.; Shen, Y.; Mu, B. Investigation of Missing-Cluster Defects in UiO-66 and Ferrocene Deposition into Defect-Induced Cavities. *Ind. Eng. Chem. Res.* **2018,** *57* (42), 14233-14241. DOI: 10.1021/acs.iecr.8b03516
56. Feng, X.; Hajek, J.; Jena, H. S.; Wang, G.; Veerapandian, S. K. P.; Morent, R.; De Geyter, N.; Leyssens, K.; Hoffman, A. E. J.; Meynen, V.; Marquez, C.; De Vos, D. E.; Van Speybroeck, V.; Leus, K.; Van Der Voort, P. Engineering a Highly Defective Stable UiO-66 with Tunable Lewis- Brønsted Acidity: The Role of the Hemilabile Linker. *J. Am. Chem. Soc.* **2020,** *142* (6), 3174-3183. DOI: 10.1021/jacs.9b13070
57. Schoenecker, P. M.; Carson, C. G.; Jasuja, H.; Flemming, C. J. J.; Walton, K. S. Effect of Water Adsorption on Retention of Structure and Surface Area of Metal–Organic Frameworks. *Ind. Eng. Chem. Res.* **2012,** *51* (18), 6513-6519. DOI: 10.1021/ie202325p
58. Canivet, J.; Bonnefoy, J.; Daniel, C.; Legrand, A.; Coasne, B.; Farrusseng, D. Structure–Property Relationships of Water Adsorption in Metal–Organic Frameworks. *New J. Chem.* **2014,** *38* (7), 3102-3111. DOI: 10.1039/C4NJ00076E
59. Ma, Y.; Cao, X.; Feng, X.; Ma, Y.; Zou, H. Fabrication of Super-Hydrophobic Film From PMMA With Intrinsic Water Contact Angle Below 90°. *Polym. J* **2007,** *48* (26), 7455-7460. DOI: 10.1016/j.polymer.2007.10.038
60. Zuo, B.; Hu, Y.; Lu, X.; Zhang, S.; Fan, H.; Wang, X. Surface Properties of Poly(vinyl alcohol) Films Dominated by Spontaneous Adsorption of Ethanol and Governed by Hydrogen Bonding. *J. Phys. Chem. C* **2013,** *117* (7), 3396-3406. DOI: 10.1021/jp3113304
61. Alamri, S.; Aguilar-Morales, A. I.; Lasagni, A. F. Controlling the Wettability of Polycarbonate Substrates by Producing Hierarchical Structures Using Direct Laser Interference Patterning. *Eur. Polym. J.* **2018,** *99*, 27-37. DOI: 10.1016/j.eurpolymj.2017.12.001
62. DeCoste, J. B.; Peterson, G. W.; Schindler, B. J.; Killops, K. L.; Browe, M. A.; Mahle, J. J. The Effect of Water Adsorption on the Structure of the Carboxylate Containing Metal–Organic Frameworks Cu-BTC, Mg-MOF-74, and UiO-66. *J. Mater. Chem. A* **2013,** *1* (38), 11922-11932. DOI: 10.1039/C3TA12497E
63. DeCoste, J. B.; Peterson, G. W.; Jasuja, H.; Glover, T. G.; Huang, Y.-G.; Walton, K. S. Stability and Degradation Mechanisms of Metal-Organic Frameworks Containing the $Zr_6O_4(OH)_4$ Secondary Building Unit. *J. Mater. Chem. A* **2013,** *1* (18), 5642-5650. DOI: 10.1039/C3TA10662D
64. Lawrence, M. C.; Schneider, C.; Katz, M. J. Determining the structural stability of UiO-67 with respect to time: a solid-state NMR investigation. *Chem. Commun.* **2016,** *52* (28), 4971-4974. DOI: 10.1039/C5CC09919F
65. Mondloch, J. E.; Katz, M. J.; Planas, N.; Semrouni, D.; Gagliardi, L.; Hupp, J. T.; Farha, O. K. Are Zr_6-Based MOFs Water Stable? Linker Hydrolysis vs. Capillary-Force-Driven Channel Collapse. *Chem. Commun.* **2014,** *50* (64), 8944-8946. DOI: 10.1039/C4CC02401J
66. Ayoub, G.; Islamoglu, T.; Goswami, S.; Friščić, T.; Farha, O. K. Torsion Angle Effect on the Activation of UiO Metal–Organic Frameworks. *ACS Appl. Mater. Interfaces* **2019,** *11* (17), 15788-15794. DOI: 10.1021/acsami.9b02764

TOC Graphic